Journal of Nano- and Electronic Physics
Vol. **18** No 5, 05020(11pp) (2026)

Журнал нано- та електронної фізики
Том **18** № 5, 05020(11cc) (2026)

OPEN ACCESS

REGULAR ARTICLE

Flexible Antenna Design for Wearable and RF Energy Harvesting in the Mid-Band Wireless Spectrum

Fahim Shahriyar, Abu Zafor Md. Touhidul Islam*

Antenna Design Lab, Department of Electrical and Electronic Engineering, University of Rajshahi, 6205 Rajshahi, Bangladesh

(Received 04 April 2026; revised manuscript received 23 October 2026; published online 28 October 2026)

The integration of polydimethylsiloxane (PDMS) into flexible RF electronics and antenna systems is advancing wearable communication technologies toward a new era. This study introduces a flexible miniaturized microstrip antenna designed for wearable devices and radio-frequency (RF) energy harvesting applications. The proposed design integrates dual parasitic elements into a planar PDMS-based patch structure, while employing Nickel–Copper (Ni–Cu) ripstop fabric as the conductor within a hybrid polymer-textile framework. The geometry enhances bandwidth and stabilizes radiation patterns without enlarging the foot-print, while the chosen materials impart flexibility, biocompatibility, and textile durability. The antenna is fully grounded with a net geometry of $20 \times 20 \times 2$ mm^3. The design is optimized in Computer Simulation Technology (CST) Microwave Studio (MWS) simulator and its performance is analyzed under the free space and on-body conditions, with the accomplishment of bending and Specific absorption rate (SAR) analyses. It operates over 5.8 GHz-6.88 GHz covering mid-band frequency spectrum which includes 5.8 GHz ISM band, 6 GHz band (WiFi 6E/7) and 5G Sub-6 GHz band, ensuring it suitable for a wide spectrum of modern wire-less communication. The antenna attains a free space return loss of − 35.269 dB and an impedance band-width of 1.08 GHz, ensuring compatibility with diverse RF energy sources. It efficiently captures RF energy with a gain of 2.473 dB at 6.06 GHz and a directivity of 6.874 dBi, while converting RF energy into electrical energy with a maximum efficiency of − 4.403 dB (38 %). An experimental prototype of the proposed antenna is fabricated, and the measured result of return loss in free space is in good agreement with the simulated one. The findings of this study contribute to the advancement of energy-autonomous wearable devices and offer valuable insights for future developments in wearable energy harvesting systems within the mid-band wireless spectrum.

Keywords: PDMS, Ni/Cu ripstop fabric, Wi-Fi 6E/7, ISM band, 5G Sub-6 GHz, Wearable, SAR, Bending Analysis, Compact antenna, Radiofrequency (RF) energy harvesting.

DOI: 10.21272/jnep.18(5).05020 PACS number: 84.40.Ba

1. INTRODUCTION

The rapid growth of wireless body area networks (WBANs) has accelerated the adoption of wearable devices in entertainment, healthcare, communications, and military applications for remote monitoring [1, 2]. Wearable antennas face challenges near the human body, including impedance detuning, reduced radiation efficiency, and elevated specific absorption rate (SAR) [3]. Effective WBAN communication requires low-profile, compact antennas with monopole-like radiation in the body's near field [4]. Military applications demand numerous sensors and electronics integrated into gear, creating the need for flexible, lightweight antennas that seamlessly fit within WBAN systems [5].

The growing demand for flexible electronics and antennas has inspired exploration of innovative materials for use as substrates [6]. Fabric substrates are popular but highly sensitive to environmental factors such as temperature and moisture, which degrade radiation performance. Polymers offer flexibility, stretchability, and conformal adaptability, with common options including polyimide (PI), liquid crystal polymers (LCP), composite laminates, and rubber-based composites, though they suffer from poor flexibility and reduced performance at high temperatures [7]. In this context, silicon-based polymer PDMS emerges as a promising substrate, offering low cost, transparency, high flexibility, customizable thickness, waterproofing, thermal stability, and isotropic properties [8, 9]. PDMS can be tailored in the lab to specific dielectric requirements and withstands bending and twisting while maintaining structural integrity and stable electromagnetic performance [10-14].

Energy harvesting (EH) derives energy from external sources to power small, wireless autonomous devices such as wearable electronics and sensor networks [15, 16]. RF EH systems harness ambient RF signals to enable device operation, yet effective RF electronics for off-body and on-body communications remain challenging. Environmental energy harvesting offers a viable solution for low-power devices, with explored sources including wind, vibration, solar, and electromagnetic

* Correspondence e-mail: touhid.eee@ru.ac.bd

© 2026 The Author(s). Journal of Nano- and Electronic Physics published by Sumy State University. This article is distributed under the terms and conditions of the Creative Commons Attribution (CC BY) license.

Cite this article as: F. Shahriyar, et al., *J. Nano- Electron. Phys.* 18 No 5, 05020 (2026) https://doi.org/10.21272/jnep.18(5).05020

waves [17]. Among these, RF energy harvesting is implantable and sustainable, providing advantages over wind, solar, and vibration methods [18-21]. Moreover, the density of RF sources in the environment has increased significantly with advances in wireless communication systems [22]. Rectennas convert RF electromagnetic waves into direct current power, enabling wireless energy harvesting for small devices. Despite extensive research, practical applications remain limited due to low DC output and frequency constraints. Multiband, broadband, and array rectennas are emerging to improve efficiency [23]. Current uses include powering implantable biomedical devices, wireless charging, and supporting WSN nodes. Integrating wearable electronics with RF wireless power transfer faces challenges, yet its potential for self-sustainability, convenience, and safety makes it a promising technology for future applications [24].

Recent advances in wireless communication standards, particularly Wi-Fi 6E, have expanded operational frequencies into the 5.925-7.125 GHz band, enabling higher capacity and reduced latency [25]. This has intensified research into antenna technology for Wi-Fi 6E and energy harvesting applications. Studies [26-30] highlight innovative miniaturized, high-gain, wideband antenna designs tailored for off-body and on-body wireless energy harvesting, reflecting a multidisciplinary approach that bridges communication and energy applications.

This study presents a flexible, compact wideband microstrip antenna employing dual parasitic elements integrated into a PDMS-based patch with Ni/Cu ripstop fabric conductors. The design achieves wideband/multiband operation across the mid-band wireless spectrum (5.8 GHz ISM, 6 GHz Wi-Fi 6E/7, and 5G Sub-6 GHz), enhancing bandwidth and radiation stability without increasing footprint. The hybrid polymer–textile system introduces flexibility, biocompatibility, and durability, making the antenna well-suited for wearable IoT, energy harvesting, and smart clothing applications. Novelty arises from structural innovation (dual parasitic coupling) and material innovation (PDMS and Ni/Cu ripstop fabric), enabling robust antennas for next-generation wearables and advancing sustainable RF energy harvesting solutions. The rest of this paper is organized as follows. Section 2 outlines the design methodology, Section 3 presents simulated and measured results, including bending and SAR analyses, and Section 5 concludes the study.

2. ANTENNA DESIGN METHODOLOGY

The design process includes several key stages such as selection of suitable materials, determination of antenna dimensions through analytical modeling, and optimization of the structure using advanced simulation tools to achieve the desired performance in terms of resonant frequency, impedance bandwidth, gain, and radiation characteristics. Initial dimensions of the antenna were calculated using the Transmission Line Model equations. The radiation performance of the proposed antenna is enhanced through a combined approach of integration of parasitic elements and systematic parametric investigation. Parasitic elements, which are passive conductors placed in close proximity to the main radiating patch, interact with the primary radiating element through mutual coupling. This interaction modifies the surface current distribution without increasing the overall antenna size and effectively extends the electrical path, enabling the antenna to support multi-resonant operation. As a result, the impedance bandwidth is broadened, gain is stabilized, and return loss is minimized across the operating frequency bands.

2.1 Materials Selection for the Proposed Antenna

The antenna consists of three primary components: the patch, the substrate, and the ground plane. The Polydimethylsiloxane (PDMS) is a silicon-based organic polymer selected as the substrate for its lightweight structure, mechanical elasticity, and excellent compatibility with flexible electronic systems. PDMS exhibits a low dielectric constant (2.7-3.0) and a low loss tangent (< 0.02), both of which contribute to enhanced antenna efficiency, minimal signal attenuation, and stable impedance characteristics over a wide frequency range.

Nickel–Copper (Ni–Cu) ripstop fabric is utilized for both the patch and the ground plane due to its high electrical conductivity, strong corrosion resistance, mechanical flexibility, and excellent compatibility with soft and stretchable substrates like PDMS. Compared to traditional copper tape, Ni–Cu conductive fabric offers enhanced durability and stability, especially in wearable and conformal antenna applications, where continuous bending, stretching, and deformation can occur. The fabric used in this study has conductivity of ≤ 0.05 Ω/sq and thickness of 0.08 mm. The fabric is cut precisely to the designed patch and ground dimensions and laminated onto the cured PDMS substrate. Combining Ni–Cu ripstop fabric with PDMS achieves an optimal balance of conductivity, flexibility, durability, and cost-efficiency.

2.2 Construction of PDMS Substrate

SYLGARD™ 184 Elastomer Kit (Dow Corning Corp.) was used for making PDMS and adapted the procedure for fabricating the PDMS composite substrate described in [31-33]. The kit contains two parts: Silicone Base (monomer) and Curing Agent. PDMS was made manually by mixing the monomer and the curing agent using a ratio of 10:1 weight ratio until a homogeneous blend was achieved. To remove trapped air bubbles formed during mixing, the PDMS mixture was placed under vacuum degassing for several minutes until no visible bubbles remained. The degassed PDMS mixture was then carefully poured into a flat mold to achieve the desired substrate geometry. The target thickness of the substrate was maintained at 2 mm. The molded PDMS mixture was subsequently heated and dried (cured) for its structural stability at a controlled temperature until fully solidified using an electric oven. After curing, the PDMS substrate was allowed to cool to room temperature, then gently removed from the mold.

2.3 Configuration of the Proposed Antenna

Fig. 1 illustrates the geometry of the proposed antenna, showing both the front and back views of the structure. It uses two parasitic elements of widths W_1

and W_2 placed alongside the main patch. Central patch defines the dominant resonance. Its length (PL) sets the fundamental frequency, while width (W_3) influences impedance and bandwidth. Parasitic Element 1 (Width W_1) and 2 (Width W_2) positioned on the opposite sides of the patch couples electromagnetically with the main patch, introducing an additional resonance close to the fundamental, broadens the operating band bandwidth and stabilizes radiation patterns. The parallel gap bars (W_3 and W_4) controls current distribution and enhance bandwidth performance. A microstrip feedline ($FW \times FL$) of length (FL) 6 mm and width (FW) 2 mm giving a 50 Ω impedance required for effective power transfer between the source and the radiating elements.

The proposed antenna is constructed on a PDMS substrate, which has a relative permittivity (ε_r) of 3, a loss tangent ($tan\ \delta$) of 0.01, and a thickness of 2 mm. The ground plane, feed line, and radiating patches are fabricated using Ni-Cu ripstop fabric, which has a thickness of 0.088 mm. The antenna was initially designed to operate at a resonant frequency of 6.06 GHz. The antenna is then modeled and simulated using CST-MWS software. After that, parametric optimization is performed to fine-tune the antenna performance. The optimized size of the antenna is $22 \times 22 \times 2$ mm^3. Once the design meets the desired results, it is fabricated and tested using a Vector Network Analyzer (VNA). The optimized geometrical parameters obtained through CST simulation are summarized in Table 1.

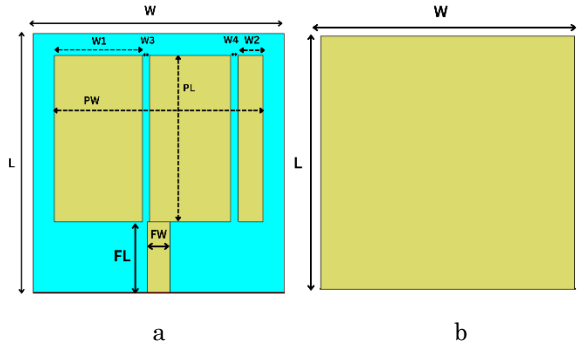


Fig. 1 – The proposed antenna's geometric structure, (a) Front view and (b) Back view

Table 1 – Optimized design parameter values

Design Parameter	Value (mm)
Ground Width (GW)	22
Ground Length (GL)	22
Substrate Width (W)	22
Substrate Length (L)	22
Patch Width (PW)	18.37
Patch Length (PL)	14.13
Width of W_1	7.71
Width of W_2	2.19
Width of W_3	0.6
Width of W_4	0.65
Width of Feedline (FW)	2
Length of Feedline (FL)	6

2.4 Parametric Investigation of Designed Antenna

The various design steps (denoted as Step 1, 2 and 3) of the proposed antenna are shown in Fig. 2 and the corresponding return loss (S_{11}) versus frequency plot is shown in Fig. 3. The design starts with a simple rectangular patch antenna (Step 1) and full ground is used in each Step. As seen, the use of parasitic elements in subsequent design steps 2 and 3 improve S_{11} of the antenna and widen the bandwidth at the expected frequency. In Step 1, the return loss is just below – 10 dB, indicating initial matching. In Step 2, it significantly decreases to – 22 dB, showing better impedance matching. Finally, in Step 3, the return loss reaches – 35.269 dB at the desired resonant frequency of 6.06 GHz, demonstrating excellent matching and minimal reflection. Additionally, the antenna bandwidth shows noticeable improvement across the steps, reflecting enhanced overall performance. All three curves dip near 6.0 GHz, indicating resonance around that point. Step 1 (black) shows shallow dip, just below – 10 dB, Step 2 (red) shows improved dip, around – 20 dB, showing better matching. Step 3 (blue) shows deepest dip, below – 30 dB, excellent matching. Step 3 provides the widest usable – 10 dB bandwidth, while Step 2 giving moderate, and Step 1 narrowest bandwidth. Thus, Step 3 achieved strong resonance and wideband operation.

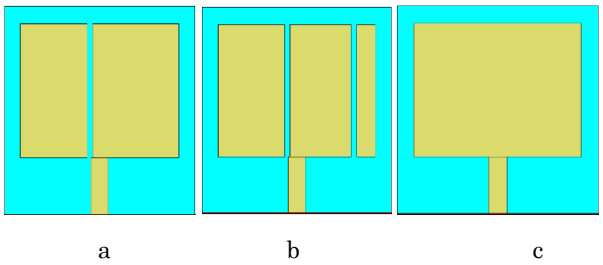


Fig. 2 – Various steps of developing the proposed antenna: (a) Step 1, (b) Step 2, and (iii) Step 3.

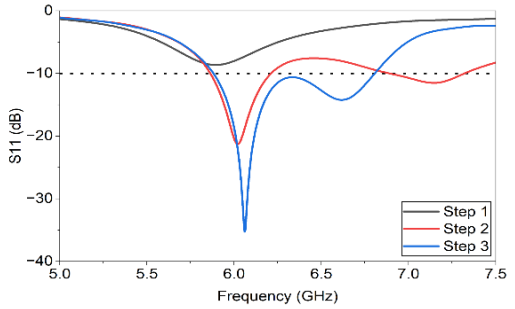


Fig. 3 – Parametric analysis of different development stages of antenna design

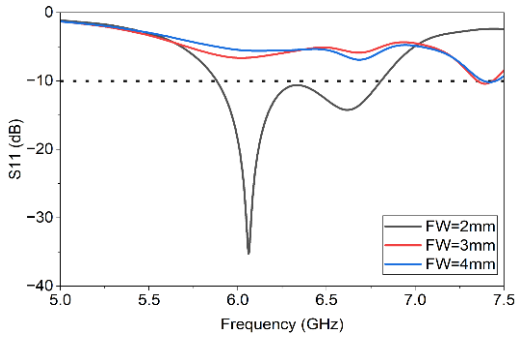


Fig. 4 – Impact of feed line width on S_{11} of the proposed antenna

Fig. 4 depicts the effect of varying the feed line width (*FW*) on the antenna's reflection coefficient across the frequency band from 5-7.5 GHz. All three curves dip around 6.0 GHz, meaning the antenna resonates there. Curve for $FW = 2$ mm (black) shows deepest dip, below – 30 dB, indicating excellent impedance matching and very low reflection compared to the wider feedlines. $FW = 2$ mm provides the widest usable bandwidth around resonance. Wider feedlines shift resonance upward and may degrade matching due to increased capacitive loading or altered current distribution. Smaller *FW* (2 mm) provides better matching, deeper resonance, wider bandwidth.

The impact of varying the ground width (*GW*) on S_{11} across 5-7.5 GHz is shown in Fig. 5. All three curves dip around 6.0 GHz, indicating resonance at that frequency. Curve for $GW = 22$ mm (black) shows deepest dip, below – 30 dB, excellent matching. $GW = 22$ mm provides the widest usable bandwidth**.** It depicts that the larger *GW* (22 mm) provides stronger resonance, better impedance matching, and wider bandwidth.

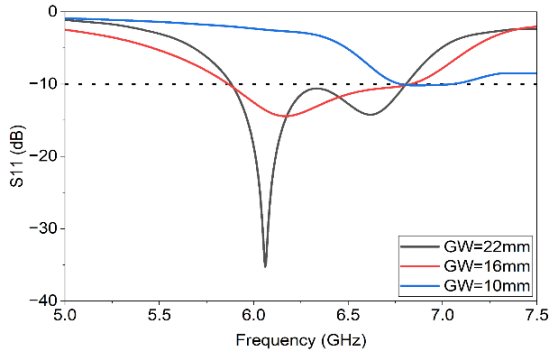


Fig. 5 – Impact of ground width on S_{11} of the proposed antenna

Fig. 6 shows how ground length (*GL*) affects the antenna's S_{11} across 5-7.5 GHz. All three curves dip near 6.0 GHz, indicating resonance around that point. As *GL* increases, the resonance depth improves, with $GL = 22$ mm showing deeper dips, meaning stronger impedance matching and reduced reflection. The dips also broaden slightly with larger *GL*, suggesting improved bandwidth. Smaller *FL* values produce sharper, narrower resonances, while larger *GL* values yield wider operational ranges. It demonstrates that longer *GL* (22 mm) provides stronger resonance, better matching, and wider bandwidth.

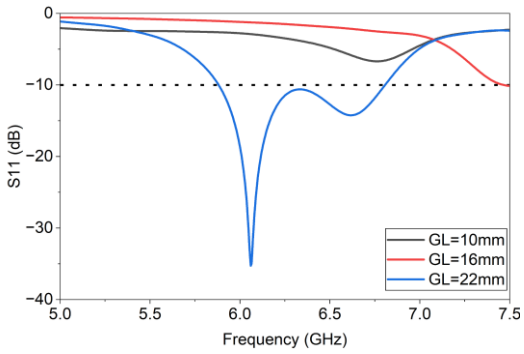


Fig. 6 – Impact of ground length on S_{11} of the proposed antenna

3. RESULTS AND DISCUSSION

The proposed antenna was simulated using CST MWS 2018 to evaluate its performance. Key parameters such as return loss (S_{11}), impedance bandwidth, VSWR, gain, directivity, efficiency, and radiation patterns were analyzed.

3.1 Off-body Simulation Results

Simulations performed under the free space or off-body condition provide the results as presented below.

3.1.1 S_{11} Parameter and VSWR

Fig. 7 depict the change in return loss (S_{11} parameter) with operating frequency of the designed antenna. It demonstrates that the antenna operates in the wide frequency range of 5.8 GHz to 6.88 GHz with return loss less than – 10 dB. The antenna exhibits two resonant peaks at 6.08 GHz and 6.625 GHz frequency where the values of return loss are – 35.269 dB and – 14.253 dB, respectively. The bandwidth is 1.08 GHz (5.8 GHz to 6.88 GHz), which covers mid-band frequency spectrum includes 5.8 GHz ISM band, 6 GHz band (WiFi 6E/7) and 5G Sub-6 GHz band, making it suitable for a wide spectrum of modern wireless communication.

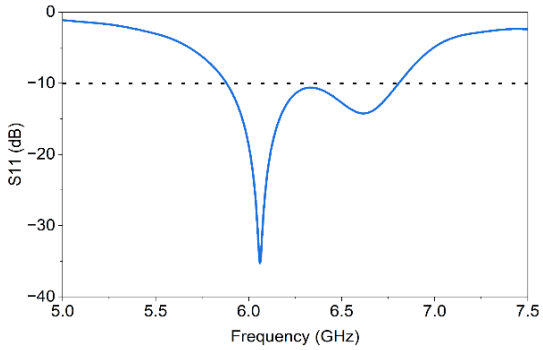


Fig. 7 – Simulated return loss (S_{11}) of the proposed antenna

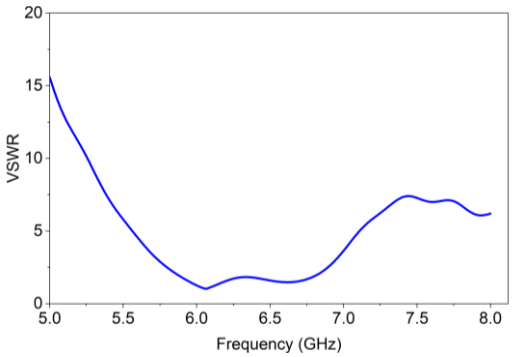


Fig. 8 – Simulated return loss of the proposed antenna

Fig. 8 presents the simulated VSWR (Voltage Standing Wave Ratio) of the proposed antenna over the frequency range 5 THz to 8 GHz. As seen, the proposed antenna achieves a VSWR value of < 2 over a wide operating frequency band (5.8 to 6.88 GHz). Thus, it realizes excellent impedance matching with efficient power transfer and minimal reflection losses, validating the antenna's suitability for wideband applications.

3.1.2 Gain and Directivity

Fig. 9 shows the 3D far-field gain pattern of the proposed antenna at the resonant frequency of 6.06 GHz. The antenna achieves a maximum directional gain of 2.473 dB, which, though modest, is typical for compact wearable and energy-harvesting designs. Its radiation efficiency of – 4.40 dB (~ 36 %) indicates the proportion of input power converted into radiation. The red/orange pattern lobes show the main radiation directions, while green/blue areas represent weaker radiation. The radiation plot confirms that the antenna radiates broadly (broad angular coverage) with moderate gain, validating the novelty of combining dual parasitic geometry with PDMS/Ni-Cu textile materials for flexible, wearable applications. For smart clothing or RF energy harvesting, the wide angular coverage is more valuable than high gain, since signals arrive from multiple directions. Efficiency is sacrificed somewhat due to material losses, but the design achieves robust, wearable friendly radiation performance.

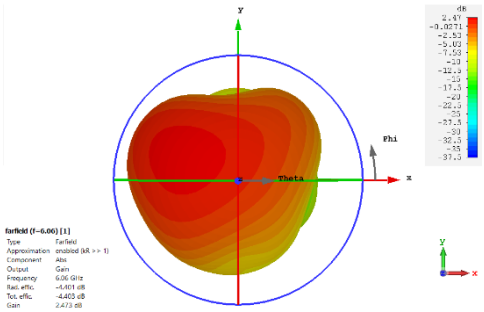


Fig. 9 – 3D farfield gain at 6.06 GHz

The 3D far-field directivity pattern of the proposed antenna at the resonant frequency of 6.06 GHz is presented in Fig. 10. At 6.08 GHz, the antenna exhibits a directivity of 6.874 dBi, indicates how strongly the antenna concentrates radiated power in its main lobe compared to an isotropic radiator. The red/orange regions represent the strongest radiation directions, while blue/green areas show weaker radiation. The spherical distribution suggests broad angular coverage rather than a sharply focused beam. At the resonant frequency of 6.06 GHz, the antenna achieves satisfactory directivity, indicating efficient radiation and strong directional performance.

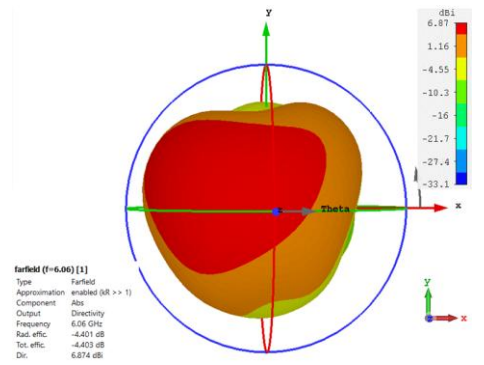
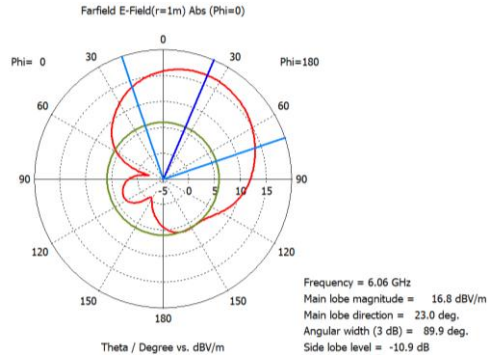


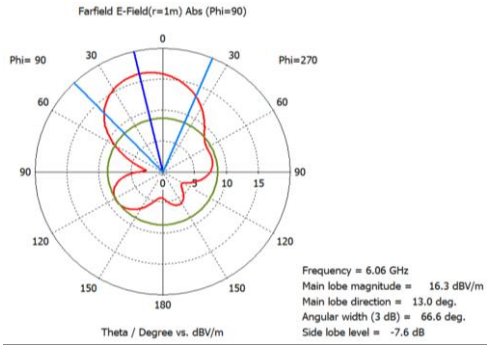
Fig. 10 – 3D Directivity at 6.06 GHz

3.1.3 Radiation Pattern

Fig. 11 presents the polar plot of the far-field electric field (E-field) at a frequency of 6.06 GHz for $\Phi = 0°$ and 90°.



a



b

Fig. 11 – 2D Farfield E-field pattern at 6.06 GHz for (a) $\varphi = 0°$ and (b) $\varphi = 90°$

As seen, the main lobe magnitudes are 16.8 dBV/m and 16.3 dBV/m, the main lobe directions are 23° and 13°, angular width (3 dB) of 89.9° and 66.6°, and side love levels are – 10.9 dB and – 6.6 dB for $\varphi = 0°$ and 90°, for $\varphi = 0°$ and 90°, respectively. For $\Phi = 0°$, the strongest radiation is 16.8 dBV/m, the antenna radiates most strongly at 23°, the main lobe spans about 89.9°, which is relatively wide, indicating a broad coverage pattern rather than a highly focused beam. The side lobes are at – 10.9 dB relative to the main lobe, showing moderate suppression. For $\varphi = 90°$, the main lobe magnitude is 16.3 dBV/m, the main lobe directions are 13°, angular width (3 dB) of 66.6°, and side love level so – 6.6 dB. Compared to the $\Phi = 0°$ cut, $\Phi = 90°$ plane shows a narrower beam, meaning higher directivity and stronger focus. The pattern is directional, concentrating energy in a specific angular region rather than radiating uniformly. Although side lobes are present, but the main lobe dominates, ensuring that most of the energy is radiated in the intended direction. With its wide beamwidth, the antenna is suitable for applications requiring coverage over a broad angular region, such as wearable devices or energy harvesting.

3.1.4 Efficiency

Fig. 12 shows the change in radiation efficiency and total efficiency with operating frequency between 4.0-

7.5 GHz. Both curves rise with frequency and reach their maximum near 6.0 GHz. At 6.06 GHz, the antenna possesses maximum radiation efficiency of 38 % and total efficiency of 37 %, providing reasonable efficiencies. After 6.0 GHz, both efficiencies decline sharply, hitting their lowest values around 7.0 GHz, before slightly recovering.

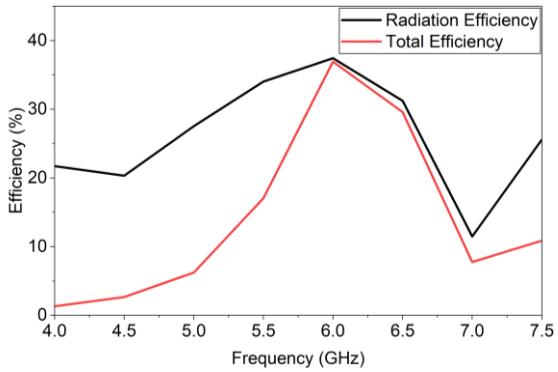


Fig. 12 – Efficiency of the proposed antenna

3.1.5 Surface Current Distribution

Fig. 13 shows the surface current density distribution on the antenna at 6.06 GHz, which reveals how currents flow across the structure when it resonates. The peak surface current density (87.7 A/m) observed in red regions near the feed and edges of the radiating patch with density. The arrows show the flow of surface currents, which align with the antenna's resonant mode. The distribution pattern confirms how energy is guided and radiated; the current originates from the microstrip line feed and spreads across the entire antenna, indicating that the whole structure contributes to resonance.

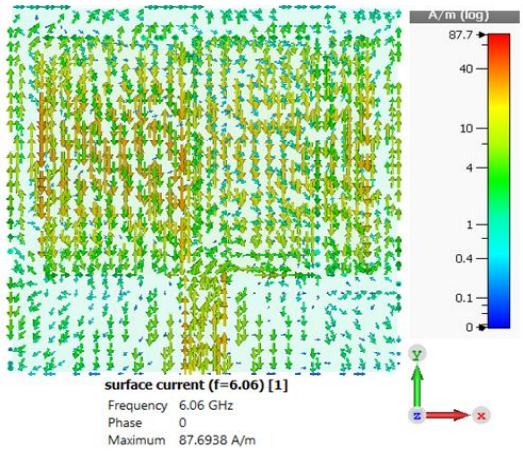
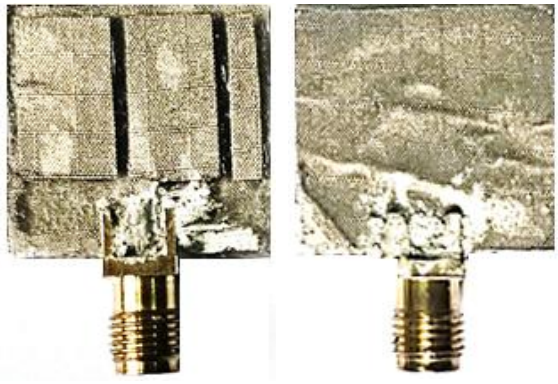


Fig. 13 – Surface current of the proposed antenna

3.2 Off-body Experimental Results

The proposed patch antenna is fabricated and its front and back views are shown in Fig. 14. Its return loss (S_{11}) parameter is measured in free space with the LiteVNA 64. Fig. 15 compares the measured and simulated reflection coefficient (S_{11}) of the antenna across 5.0-7.5 GHz. Both measured (blue dash dot) and simulated (red solid) curves dip near 6.0 GHz (measured resonance at 5.96 GHz), confirming resonance at that frequency. Simulation shows a deeper minimum (below – 35 dB), indicating excellent matching in the model. Measurement shows a shallower dip (around – 30 dB), still good but less ideal. The overall shapes of the curves align well, meaning the simulation accurately predicts the antenna's behavior. The difference in resonance frequency and depth in return loss is typical, caused by fabrication tolerances, material imperfections, or measurement setup losses.



a b

Fig. 14 – (a) Front and (b) back view of the fabricated antenna

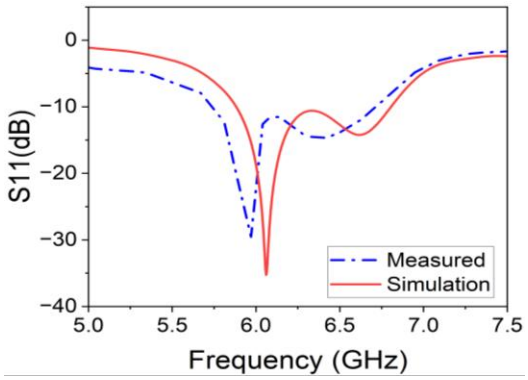


Fig. 15 – Off-body Simulation vs Experimental Return Loss comparison

3.3 On Body Simulation Results

At higher frequencies, human tissues absorb and reradiate part of the electromagnetic energy, which can significantly affect antenna parameters such as resonance frequency, bandwidth, and radiation pattern. Furthermore, bending analysis and SAR analysis are performed under the on-body condition. As the proposed antenna is intended for wearable applications, its on-body performance is evaluated on human body phantom and presented here.

3.3.1 3D Phantom Model Creation and Analysis

A three-layer human body tissue equivalent phantom model is created in CST with overall dimensions of 25 mm × 35 mm × 36 mm using three tissue layers of skin, fat, and muscle with thicknesses of 1 mm, 10 mm, and 25 mm, as shown in Fig. 16. The electrical properties of each layer are determined at 6.06 GHz by using published reports presented in [34, 35] as depicted in Table 2, is used for the simulation.

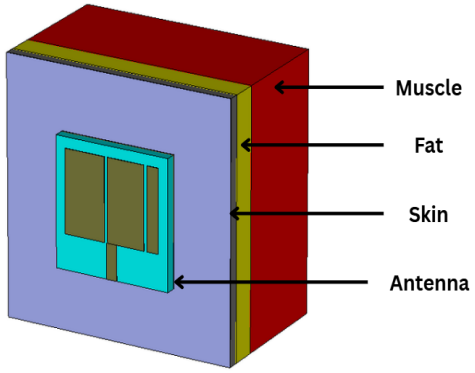


Fig. 16 – Body Phantom model

Table 2 – Model parameters at 6.06 GHz

Tissue	Thickness (mm)	Permittivity	Loss Tangent (s/m)	Mass density (Kg/m^3)
Skin	2	34.946	0.3336	1109
Fat	5	4.9367	0.18584	911
Muscle	20	48.217	0.32321	1090

Fig. 17 presents a comparison between the on-body and off-body simulation results of the antenna's return loss. The plots show strong alignment between them, demonstrating that the antenna maintains stable performance in both scenarios, confirming its reliability for wearable applications. Both conditions show two resonant dips - one near 6.0 GHz and another near 6.7 GHz, where reflection is minimized. Off body (red) plot shows deeper dips, especially at 6.08 GHz, indicating better impedance matching when the antenna is free space mounted. On body (black) plot shows shallower dips, showing degraded matching due to body loading effects. Off body provides wider usable bandwidth (below – 10 dB line). On body bandwidth is narrower, meaning reduced tolerance to frequency variation.

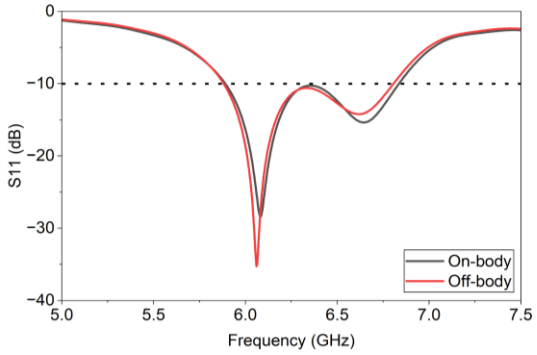


Fig. 17 – Return loss (S_{11}) under the on-body and off-body conditions

3.4 Bending Analysis

To evaluate the performance of the proposed antenna under various bending conditions on the human body or conformal surfaces, it is subjected to six distinct bending angles (0°, 15°, 30°, 45°, and 60°) over the *x*-axis. The antenna geometries are presented in Fig. 18, while the dependence of return loss on bending conditions is illustrated in Fig. 19. 0° (flat) bend results in deep resonance dip and best matching, while 15° and 30° bending plots show slight upward shift in resonance frequency, but still remains below – 10 dB, indicating performance remains acceptable. Resonance dip becomes shallower for 45° bend, showing reduced matching. Lastly, 60° bend is the worst case where resonance is weaker, reflection increases, but still maintains operation near 6.2 GHz. Thus, bending analysis demonstrates that, the antenna maintains resonance around 6.0-6.5 GHz across all bending angles, showing robust frequency stability. As bending increases, the S_{11} dip becomes shallower, meaning impedance mismatch grows. This is expected due to current redistribution and substrate deformation. Even at 60° bending, the antenna still operates near its design band, which is a strong indicator of mechanical robustness.

It is also seen from Fig. 18 that the resonant frequency shifts slightly to the left with the increase of bending angles, which may be caused by the change in antenna's geometry and path of surface current flow in the bent form. These results are consistent with other studies conducted in bending conditions [36, 37]. Even with this change in resonant peaks, the proposed antenna is remaining to operate within the specified frequency range.

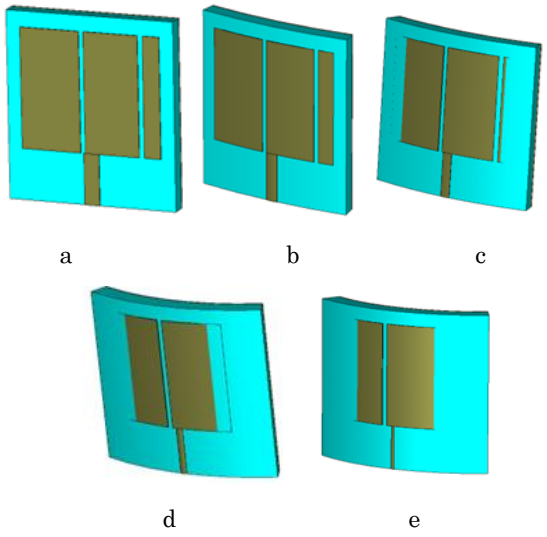


Fig. 18 – Antenna under bending angles over x-axis: (a) 0, (b) 15, (c) 30, (d) 45, (e) 60 degrees

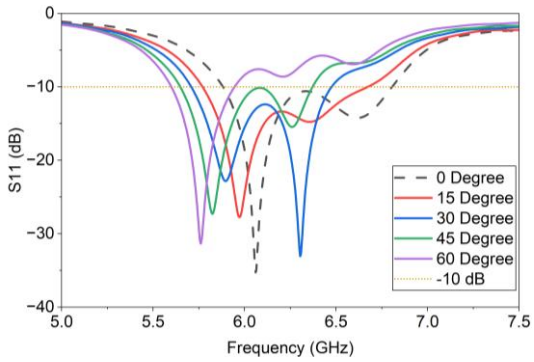


Fig. 19 – Return loss Vs. frequency of the proposed antenna under bending

Table 3 presents the values of key performance paramours of the antenna under various degrees of bending. The antenna maintains a stable resonant frequency and good impedance matching even under different

bending conditions, with slight variations in return loss. Frequency shifting is a common, but it remains within the target band. Furthermore, the gain remains almost unaffected, indicating consistent performance. Bending can disperse radiation patterns, leading to a slight drop in peak gain depending on the plane of the bend (E-plane or H-plane). The operational bandwidth shows minimal reduction, confirming that the antenna can reliably operate over its designated frequency range even when deformed. These findings validate that the proposed antenna exhibits mechanical flexibility and robust electromagnetic performance, making it suitable for wearable communication systems, where stable operation under bending and body movement is critical for reliable connectivity and signal integrity.

Table 3 – Performance under bending conditions

Bending Angle (degree)	f_o (GHz)	Retun loss (dB)	Bandwidth (GHz)	Gain (dB)
0	6.06	– 35.269	1.08 (5.80-6.88)	2.473
15	5.98	– 27.764	0.96 (5.76-6.72)	2.432
30	5.92	– 33.069	0.78 (5.71-6.48)	2.425
45	5.84	– 27.304	0.75 (5.65-6.4)	2.414
60	5.78	– 31.348	0.35 (5.6-5.95	2.403

3.5 SAR Analysis

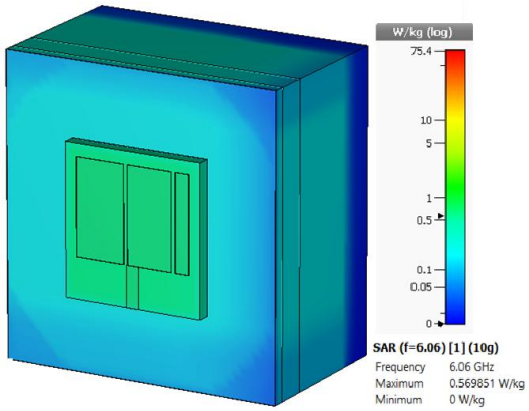


Fig. 20 – SAR analysis at 6.06 GHz for 10 g of biological tissue

Specific Absorption Rate (SAR) analysis was conducted to evaluate the safety of the proposed antenna on the human body. The SAR value was calculated according to the IEEE C95.3 standard over 10 g of biological tissue at the 6.06 GHz resonant frequency using a three-layer flat body phantom model. Simulations performed in CST with an input power of 20 mW yielded a maximum average SAR of 0.5698 W/kg, which is well below the ICNIRP safety limit of 2 W/kg. The SAR distribution on the phantom model is shown in Fig. 20.

3.6 Comparison of Proposed Antenna with Existing Researches

Table 4 shows a comparison of the proposed antenna to various existing antennas published in previous studies. Most PDMS based designs use pure copper, conductive fibers, or liquid metals (EGaIn). The present design uniquely integrates Ni Cu ripstop fabric, which is mechanically robust, lightweight, and inherently flexible. At $22 \times 22 \times 2$ mm^3, it is significantly smaller than other designs (e.g., Ref [41] at $50 \times 40 \times 1.6$ mm^3, Ref [45] at $147 \times 147 \times 6$ mm^3). This compact footprint makes it more suitable for wearable integration in constrained spaces. It resonates at 6.06 GHz, which is directly targeting mid band wireless frequencies. Bandwidth of 1.08 GHz is moderate, which is wider than textile/silver fabric (Ref [44]: 0.242 GHz), but narrower than optimized PDMS/Cu (Ref [39]: 3.7-6.25 GHz). Gain (2.47 dBi) and efficiency (38 %) of this design are modest compared to high-performance polyester or PDMS/Cu designs, but acceptable for compact wearable energy harvesting. Furthermore, SAR value of 0.5698 W/kg for 10 g of tissue is higher than ultra-low polyester (0.0003 W/kg) but much safer than Kapton/Graphene (4.6 W/kg). This positions the proposed design as safe for wearables, though optimization could reduce SAR further. While the efficiency (38 %) and SAR values are not yet optimal compared to other designs, the small footprint and resonance at 6.06 GHz make it a promising candidate for integration into smart clothing and body-centric systems.

Table 4 – Comparison of proposed antenna with earlier works

Ref	Substrate/ Conductor	Size (mm^3)	fo (GHz)	Bandwidth (GHz)	Gain (dB)	Efficiency (%)	SAR (W/Kg)
38	PDMS/Cu	35×25×2	3.5	3.28 (2.53 to 5.81)	2.58	78.59	0.134 (1g)
39	PDMS/Cu	25×25×0.5	4.25	3.7-6.25	4.20 dBi	97.5	0.15 (10g)
40	Polyester/ Cu fabric	14×22 ×0.58	5.8	5.7–7.1	8.92 dBi	80	0.0003 (10 g)
41	PDMS/Cu	50×40×1.6	5, 5.8, 6.6	4.43–6.1	6.20 dBi	70-85	0.04 (1 gm)
42	Kapton / Graphene	30×20×0.1 25	5.5	5-6	–0.35	42	1.2 (10 g)
43	PDMS/Cu	20 ×15×1.6	6.2	1.225	3.50	NR	NR
44	Textile /Ag fabric	200×200 ×50	5.8	0.242	3.66	85 to 93.2	NR
45	PDMS / EGaIn	147×147 ×6.035	2.4, 5.8	0.278	6.08 dBi	70-85	0.043 (10g)
This work	PDMS/ Ni-Cu ripstop fabric	22×22×2	6.06	1.08	2.47	38	0.5698 (10g)

Abbreviation: NR for Not Reported

For wearables, maintaining low SAR is critical to user safety, and even moderate gain ensures reliable communication in short-range networks. For energy harvesting, even moderate gain at mid-band frequencies allows effective capture of ambient Wi-Fi and cellular signals, contributing to self-powered systems. Compared to peers, this work demonstrates a practical trade-off: while not the highest in efficiency or lowest in SAR, it establishes a baseline design that can be optimized further for safe, efficient, and flexible mid-band wearable antennas. In essence, it underscores the importance of compact, flexible geometries as a foundation for next-generation wearable and energy harvest-

ing platforms. Thus, this work provides a foundation for further optimization to achieve antennas that are not only safe and comfortable for continuous wear but also capable of contributing to self-powered wearable ecosystems. The realization of moderate bandwidth, good impedance matching and I_{ow} SAR values under the on-body condition make the antenna a promising candidate for prospective WBAN applications. The proposed antenna is expected to have potential applications in various RF energy harvesting systems and portable devices due to its flexibility, low cost, low feed network loss, and robust performance. The findings contribute to the development of energy-autonomous wearable devices and provide insights for future advancements in wearable energy harvesting systems.

4. CONCLUSION

This paper presents the design of a flexible and compact microstrip patch antenna optimized for wearable communication and RF energy harvesting applications. Operating across 5.8-6.88 GHz, it covers the mid-band wireless spectrum, including the 5.8 GHz ISM band, the 6 GHz WiFi 6E/7 band, and the 5G Sub-6 GHz band. The proposed antenna, with dimensions of $20 \times 20 \times 2$ mm^3, represents a new design paradigm that combines parasitic-loaded geometry with a hybrid polymer–textile material system. Dual parasitic elements introduce coupled resonances that broaden bandwidth and enable multi-band operation and their symmetric placement stabilizes radiation patterns. The materials combination PDMS and Ni/Cu ripstop fabric introduce flexibility, biocompatibility, and textile durability. The proposed antenna achieving a return loss of – 35.269 dB with VSWR of 1.0369, and a wide impedance bandwidth of 1.08 GHz (5.8 GHz-6.88 GHz), achieving a gain of 2.473 dB. It also exhibits a radiation efficiency of 38 % (– 4.403 dB), making it suitable for both wearable and energy harvesting applications. Experimental validation showed good agreement between measured and simulated results, ensuring design reliability. Furthermore, the antenna maintains stable radiation characteristics under on-body and bending conditions, highlighting its robustness for wearable use. The estimated maximum SAR value of 0.5698 W/kg (averaged over 10 g of tissue at 6.06 GHz) is well below the IEEE safety limit of 2 W/kg, confirming its safety for human use. The realization of moderate bandwidth, good impedance matching and low SAR values under the on-body condition make the antenna a promising candidate for prospective WBAN applications. This work provides a foundation for further optimization to achieve antennas that are not only safe and comfortable for continuous wear but also capable of contributing to self-powered wearable ecosystems.

Future work will focus on optimizing the antenna structure to achieve higher gain and efficiency while reducing the SAR value. Antenna's return loss, gain, radiation patterns, efficiency, and SAR measurements will be performed in an anechoic chamber. In addition, advanced parasitic structures will be explored to achieve wider impedance bandwidths for additional bands, while alternative conductive materials will be investigated to minimize losses and enhance radiation efficiency. To maximize RF-to-DC conversion efficiency in IoT and wearable devices, the antenna will be integrated with rectifier circuits (rectennas) and impedance-matching networks.

AKNOWLEDGEMENTS

The authors would like to express gratitude to university for providing the resources and support necessary for this research. Authors also grateful for the guidance and encouragement from colleagues who have contributed valuable insights during the development of this work. Their support has been invaluable in completing this study.

REFERENCES

1. M. Yuan, R. Das, E. Mcglynn, R. Ghannam, Q.H. Abbasi, H. Heidari, *IEEE Sens J.* **21** No 11, 12484 (2021) https://doi.org/10.1109/JSEN.2021.3055077.
2. D. Chaturvedi, S. Raghavan, *Def. Sci. J.* **68** No 2, 190 (2018) https://doi.org/10.14429/dsj.68.11833.
3. F.R. Kareem, et al., *IEEE Sens J.* **23** No 19, 23377 (2023) https://doi.org/10.1109/JSEN.2023.3305917.
4. D.G. Kang, J. Tak, J. Choi, *Microw. Opt. Technol. Lett.* **58** No 5, 1093 (2016) https://doi.org/10.1002/mop.29749.
5. P.K. Sharma, N. Gupta, *IEEE J. Flex. Elect.* **1** No 1, 39 (2022) https://doi.org/10.1109/JFLEX.2022.3153240.
6. A. Ashyap, et al., *IEEE Access* **13**, 22590 (2025) https://doi.org/10.1109/ACCESS.2025.3536525.
7. A. Al-Sehemi, A. Al-Ghamdi, N. Dishovsky, G. Atanasova, N. Atanasov, *IET Microw., Antennas Propag.* **15** No 1, 80 (2021) https://doi.org/10.1049/mia2.12016.
8. P.K. Sharma, N. Gupta, P.I. Dankov, *AEU Int. J. Electron. Commun.* **127**, (2020) https://doi.org/10.1016/j.aeue.2020.153455.
9. A.A. Bakar, F. Hasnan, A.R. Razali, A.F.A. Rahim, M.S. Osman, T. Ali, R. Radzali, *Acta Phys. Polonica A* **135** No 5, 938 (2019) https://doi.org/10.12693/APhysPolA.135.938.
10. P.K. Sharma, N. Gupta, P.I. Dankov, *IEEE Sensors J.* **21** No 17, 19492 (2021) https://doi.org/10.1109/JSEN.2021.3089827.
11. S. Sankaralingam, B. Gupta, *IEEE Trans. Instrum. Meas.* **59** No 12, 3122 (2010) https://doi.org/10.1109/TIM.2010.2063090.
12. T.T. Le, T.Y. Yun, *IEEE Antennas Wireless Propag. Lett.* **24** No 7, 1175 (2021) https://doi.org/10.1109/LAWP.2021.3074641.
13. G. Gao, et al., *IEEE Antennas Wireless Propag. Lett.* **24** No 7, 1719 (2025) https://doi.org/10.1109/LAWP.2025.3545640.
14. R. Simorangkir, et al., *IEEE Antennas Wireless Propag. Lett.* **17** No 3, 493 (2018) https://doi.org/10.1109/LAWP.2018.2797251.
15. S.S. Ojha, P.K. Singhal, V.V. Thakare, *Meas. Sens.* **24**, 100532 (2022) https://doi.org/10.1016/j.measen.2022.100532.
16. S.E. Adami, P. Proynov, G.S. Hilton, G. Yang, C. Zhang, D. Zhu, Y. Li, S.P. Beeby, I.J. Craddock, B.H. Stark, *IEEE Trans. Microw. Theory Tech.* **66**, 380 (2018) https://doi.org/10.1109/TMTT.2017.2700299.
17. B.Y. Yu, Z.H. Wang, L. Ju, C. Zhang, Z.G. Liu, L. Tao, W.B. Lu, *IEEE Trans. Antenn. Propag.* **70** No 3, 2223 (2021) https://doi.org/10.21272/jnep.15(3).03010.
18. M. Dini, A. Romani, M. Filippi, V. Bottarel, G. Ricotti, M. Tartagni, *IEEE Trans. Power Elecron.* **30** No 10, 5665 (2015) https://doi.org/10.1109/TPEL.2014.2379622.
19. A. Eddiai, M. Meddad, M.H. Mazroui, Y. Boughaleb,

M. Idiri, R. Khanfer, M. Rguiti, *Polym. Adv. Technol.* **27** No 5, 677 (2016) https://doi.org/10.1002/pat.3738.
20. M. Piñuela, P.D. Mitcheson, S. Lucyszyn, *IEEE Trans. Microwave Theory Tech.* **61** No 7, 2715 (2013) https://doi.org/10.1109/TMTT.2013.2262687.
21. M. Boutaldat, N. Chakhchaoui, A. Eddiai, M. Meddad, O. Cherkaoui, M. Rguiti, M.H. Mazroui, *Polym. Adv. Technol.* **33** No 10, 3216 (2022) https://doi.org/10.1002/pat.5773.
22. Q. Awais, Y. Jin, H.T. Chattha, M. Jamil, H. Qiang, B.A. Khawaja, *IEEE Access* **6**, 35857 (2018) https://doi.org/10.1109/ACCESS.2017.
23. C. Song, Y. Huang, J. Zhou, J. Zhang, S. Yuan, P. Carter, *IEEE Trans. Anten. Propag.* **63** No 8, 3486 (2015) https://doi.org/10.1109/TAP.2015.2431719.
24. Y. Lu, M.C. Biswas, Z. Guo, J.-W. Jeon, E.K. Wujcik, *Biosens. Bioelectron.* **123**, 167 (2019) https://doi.org/10.1016/j.bios.2018.08.037.
25. E. Mozaffariahrar, F. Theoleyre, M.Menth, *Future Internet.* **14**, 293 (2022) https://doi.org/10.3390/fi14100293.
26. Z. Yunusa, *International Journal of Innovative Technology and Exploring Engineering* **13**, 21 (2024) https://doi.org/10.35940/ijitee.h9919.13070624.
27. F. Alam, M.A. Islam, M.F. Ahmed, M.M. Islam, M.H. Kabir, *International Conference on Recent Progress-es in Science, Engineering and Technology* (ICRPSET), 1 (2022) https://doi.org/10.1109/ICRPSET57982.2022.10188500.
28. R.H. Masum, M.A. Islam, S.C. Roy, M.F. Ahmed, M.M. Islam, M.R. Hossain, R. Sarkar, *Cureus Journals* (2025) https://doi.org/10.7759/s44388-024-02717-3.
29. M.S.S. Kumar, M. Bharath, J. Das, B.R.S. Reddy, G. Srinivas, G.S. Teja, *International Conference on Distributed Computing and Optimization Techniques* (ICDCOT), 1 (2024) https://doi.org/10.1109/icdcot61034.2024.10515455.
30. F. Yang, S. Chaoyun, H. Yichao, 4th *URSI Atlantic Radio Science Meeting* (AT-RASC), (2024) https://doi.org/10.46620/ursiatrasc24/lpri8860.
31. Z. Lanlin, W. Zheyu, J.L. Volakis, *IEEE Antennas and Wireless Propagation Letters* **11**, 1690 (2012) https://doi.org/10.1109/LAWP.2013.2239956.
32. S. Koulouridis, G. Kiziltas, Z. Yijun, D.J. Hansford, J.L. Volakis, *IEEE Transactions on Microwave Theory and Techniques* **54** No 12, 4202 (2006) https://doi.org/10.1109/TMTT.2006.885887.
33. J.C. McDonald, G.M. Whitesides, *Accounts of Chemical Research* **35** No 7, 491 (2002) https://doi.org/10.1021/ar010110q.
34. P.A. Hasgall, F. Di Gennaro, C. Baumgartner, et al., *Version* **4.1**, (2022) https://doi.org/10.13099/VIP21000-04-1.
35. http://niremf.ifac.cnr.it/tissprop/htmlclie/htmlclie.php.
36. A. Mersani, L. Osman, J.M. Ribero, *Proc. of 18th Mediterranean Microwave Symposium MMS*, 255 (2018) https://doi.org/10.1109/MMS.2018.8612049.
37. S.M. Salleh, M.F. Ain, Z. Ahmad, et al., *Express Polymer Letters* **16** No 12, 1267 (2022) https://doi.org/10.3144/expresspolymlett.2022.92.
38. Md. Mehedi Hasan, Abu Zafor Muhammad Touhidul Islam, *Cureus J. Eng.* **2**, es44388-025-04462-7 (2025) https://doi.org/10.7759/s44388-025-04462-7.
39. Musa Hussain, Wahaj Abbas Awan, Syed Muzahir Abbas, Yong Zhu, *Results in Engineering* **25**, 103818 (2025) https://doi.org/10.1016/j.rineng.2024.103818.
40. W. Bouamra, I. Sfar, A. Mersani, L. Osman, J.-M. Ribero, *Eng. Technol. Appl. Sci. Res.* **12** No 4, 9048 (2022) https://doi.org/10.48084/etasr.5011.
41. P.K. Sharma, N. Gupta, *IEEE J. Flex. Electron.* **1** No 1, 39 (2022) https://doi.org/10.1109/JFLEX.2022.3153240.
42. I.I. Labiano, A. Alomainy, *Flex. Print. Electron.* **6** No 2, 025010 (2021) https://doi.org/10.1088/2058-8585/ac0ac1.
43. Tilakdhari Singh, Pooja Sharma, Shivesh Tripathi, Vijay Shanker Tripathi, *Defence Science Journal* **74** No 4, 546 (2024) https://doi.org/10.14429/dsj.74.19018.
44. R.B.V.B. Simorangkir, Y. Yang, L. Matekovits, K.P. Esselle, *IEEE Ant. Wire. Propag. Lett.* **16**, 677 (2016) https://doi.org/10.1109/LAWP.2016.2598729.
45. Muhammad Nazrin Ramli, Ping Jack Soh, Mohd Faizal Jamlos, Herwansyah Lago, Norazizan Mohd Aziz, Al-Hadi Azremi Abdullah, *Appl. Phy. A* **123** No 149, (2017) https://doi.org/10.1007/s00339-017-0754-3.
46. Zhenzhen Jiang, Zijian Dong, Pengfei Song, Mark Leach, Yi Huang, *IEEE Antennas and Wire-less Propagation Letters* **25** No 5, 2235 (2026) https://doi.org/10.1109/LAWP.2026.3676083.

Конструкція гнучкої антени для ношуваних пристроїв та збору радіочастотної енергії у середньому діапазоні бездротового спектра

Fahim Shahriyar, Abu Zafor Md. Touhidul Islam

Antenna Design Lab, Department of Electrical and Electronic Engineering, University of Rajshahi, 6205 Rajshahi, Bangladesh

Інтеграція полідиметилсилоксану (ПДМС) у гнучку радіочастотну (РЧ) електроніку та антенні системи відкриває нову еру в розвитку технологій зв'язку для ношуваних пристроїв. У цьому дослідженні представлено гнучку мініатюрну мікросмужкову антену, розроблену для ношуваних пристроїв та систем збору радіочастотної енергії. Запропонована конструкція поєднує два паразитні елементи з планарною структурою на основі ПДМС, причому як провідник у гібридній полімерно-текстильній системі використовується тканина типу «ріпстоп» із нікель–мідним (Ni–Cu) покриттям. Така геометрія дозволяє розширити смугу пропускання та стабілізувати діаграму спрямованості без збільшення габаритів антени, а обрані матеріали забезпечують гнучкість, біосумісність і довговічність, притаманну текстильним виробам. Антена має суцільний шар заземлення, а її загальні розміри становлять 20 × 20 × 2 мм^3. Конструкцію було оптимізовано в середовищі моделювання CST Microwave Studio (MWS); також було проаналізовано її характеристики як у вільному просторі, так і при розміщенні на тілі людини, зокрема досліджено вплив вигинання та визначено питомий коефіцієнт поглинання (SAR). Антена працює в діапазоні частот від 5,8 ГГц до 6,88 ГГц, що охоплює середньочастотний спектр (зокрема діапазон ISM 5,8 ГГц, діапазон 6 ГГц для стандартів WiFi 6E/7 та діапазон 5G Sub-6 ГГц), що робить її придатною для широкого спектра сучасних систем бездротового зв'язку. У вільному просторі антена демонструє зворотні втрати на рівні − 35,269 дБ та смугу пропускання за імпедансом 1,08 ГГц, що забезпечує сумісність із різними джерелами радіочастотної енергії. Вона ефективно вловлює РЧ-

енергію, маючи коефіцієнт підсилення 2,473 дБ на частоті 6,06 ГГц і спрямованість 6,874 дБі, при цьому перетворюючи РЧ-енергію на електричну з максимальною ефективністю − 4,403 дБ (38 %). Було виготовлено експериментальний зразок антени; результати вимірювань зворотних втрат у вільному просторі добре узгоджуються з даними комп'ютерного моделювання. Результати цього дослідження сприяють розвитку енергоавтономних ношуваних пристроїв і надають важливі дані для подальших розробок у сфері систем збору енергії для ношуваної електроніки, що працює в середньочастотному діапазоні бездротового зв'язку.

Ключові слова: PDMS, Тканина типу «ріпстоп» із покриттям Ni/Cu, Wi-Fi 6E/7, Діапазон ISM, 5G (діапазон до 6 ГГц), SAR, Аналіз впливу вигинів, Компактна антена, Збір радіочастотної (РЧ) енергії.